

Atomic Layer Deposition of Lithium Niobium Oxides as Potential Solid-State Electrolytes for Lithium-Ion Batteries

Biqiong Wang,^{†,‡} Yang Zhao,^{†,‡} Mohammad Norouzi Banis,[†] Qian Sun,[†] Keegan R. Adair,[†] Ruying Li,[†] Tsun-Kong Sham,^{*,‡} and Xueliang Sun^{*,†,‡}

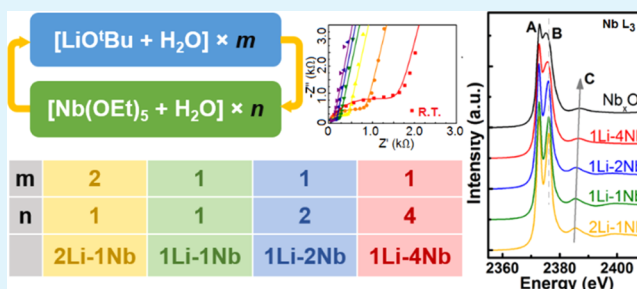
[†]Department of Mechanical and Materials Engineering, University of Western Ontario, London, Ontario N6A 5B9, Canada

[‡]Department of Chemistry, University of Western Ontario, London, Ontario N6A 5B7, Canada

Supporting Information

ABSTRACT: The development of solid-state electrolytes by atomic layer deposition (ALD) holds unparalleled advantages toward the fabrication of next-generation solid-state batteries. Lithium niobium oxide (LNO) thin films with well-controlled film thickness and composition were successfully deposited by ALD at a deposition temperature of 235 °C using lithium *tert*-butoxide and niobium ethoxide as Li and Nb sources, respectively. Furthermore, incorporation of higher Li content was achieved by increasing the Li-to-Nb subcycle ratio. In addition, detailed X-ray absorption near edge structure studies of the amorphous LNO thin films on the Nb L-edge revealed the existence of Nb as Nb⁵⁺ in a distorted octahedral structure. The octahedrons in niobium oxide thin films experienced severe distortions, which could be gradually alleviated upon the introduction of Li atoms into the thin films. The ionic conductivities of the as-prepared LNO thin films were also measured, with the highest value achieving $6.39 \times 10^{-8} \text{ S cm}^{-1}$ at 303 K with an activation energy of 0.62 eV.

KEYWORDS: lithium niobium oxide, atomic layer deposition, solid-state electrolyte, lithium-ion battery, X-ray absorption spectroscopy



INTRODUCTION

Lithium-ion batteries (LIBs) have been the subject of extensive studies in the past decades for a wide range of applications including portable electronics, electric vehicles, and grid energy storage systems. However, the increasing demands of technological advancements require safer and longer-lasting battery systems with a higher energy density.^{1–4} One of the most promising avenues is the development of all solid-state batteries (ASSBs). The direct replacement of flammable liquid electrolytes used in conventional LIBs with solid-state electrolytes (SSEs) can significantly reduce the inherent safety risks that might lead to catastrophic battery failures. Additionally, SSEs provide better thermal stability, increased electrochemical stability, and, in some cases, wider voltage windows.^{5–7} Furthermore, SSEs allow for conceptual innovations in battery design, enabling the switch from two-dimensional liquid electrolyte batteries to three-dimensional (3D) ASSBs. In those proposed designs, the vastly increased surface area allows for higher energy densities in a limited areal footprint, whereas the short diffusion paths can enable good power density.^{8–11}

However, the fabrication process of 3D ASSBs has significant challenges that need to be addressed. The SSEs must be deposited homogeneously and uniformly over a substrate with a high aspect ratio, which can only be achieved by atomic layer deposition (ALD).^{12–14} Compared to physical deposition techniques like pulsed laser deposition or sputtering, ALD is

based on chemical reactions where the vapor-phase precursors are alternatively pulsed into the reaction chamber and react in a self-limiting manner. The self-limiting surface reactions enable precise control over film thickness and guarantees excellent coverage and uniformity on the substrates.^{15–19} In recent times, there have been significant efforts dedicated to the development of ALD processes of lithium-containing compounds for SSE materials. Lithium carbonate was first successfully synthesized by Putkonen et al., who initiated a great leap forward in the development of lithium-containing systems by ALD.²⁰ Subsequently, several SSE materials such as lithium lanthanum titanate, lithium alumina, lithium tantalate, lithium phosphate, lithium lanthanum zirconia (LLZO), and lithium phosphorus oxynitride (LiPON) have been reported.^{21–30} Among the inorganic SSEs, crystalline systems such as LLZO would require drastic postheat treatment, which could lead to severe problems in the measurement of ionic conductivity and even the fabrication of ASSBs.^{22,24,27} In addition, it is difficult to obtain a pure phase SSE without carefully tuning the composition of the as-prepared materials. Therefore, glassy SSEs attract more attention due to the fact that they require no further annealing. Among the potential candidates, LiPON has

Received: September 5, 2017

Accepted: December 8, 2017

Published: December 8, 2017

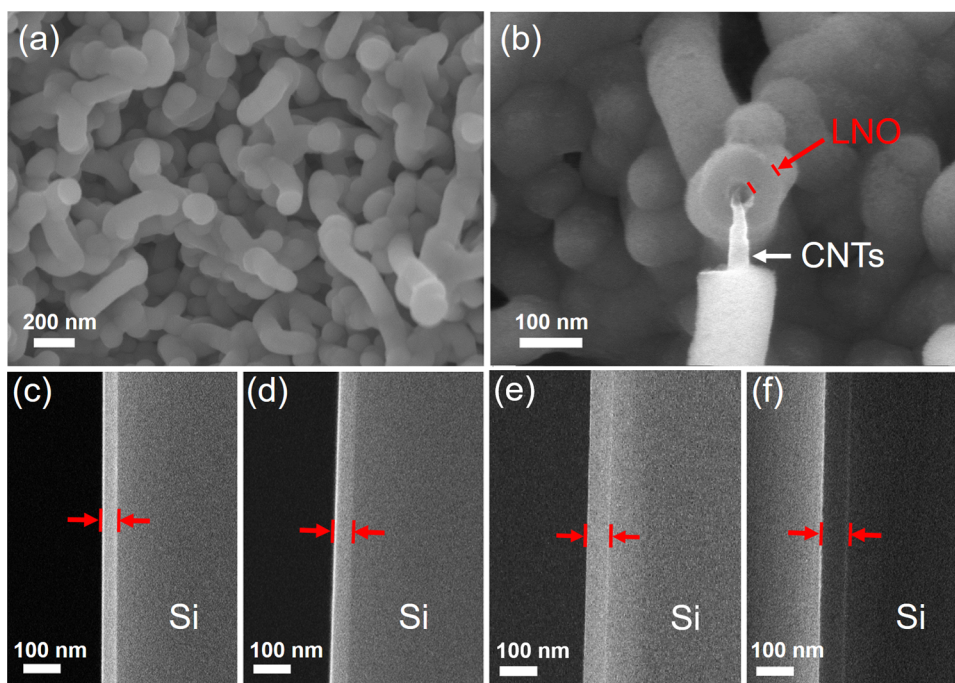


Figure 1. SEM morphology of lithium niobium oxide thin films after 250 cycles at 235 °C: (a, b) 1Li-1Nb on CNTs, (c-f) cross-sectional views of 1Li-1Nb, 1Li-2Nb, 1Li-4Nb, and 2Li-1Nb on Si substrates. LNO thin films are highlighted with red arrows.

been one of the most popular SSEs for thin-film batteries. Recently, ALD processes of LiPON thin films have been established whose conductivity can reach as high as 10^{-7} S cm^{-1} at room temperature.^{14,28–30}

Apart from the aforementioned SSE materials, lithium niobate glasses have demonstrated good ionic conductivity. Lithium ions can move isotropically in the randomly cross-linked glass networks, giving a conductivity of 10^{-5} – 10^{-9} S cm^{-1} under different synthesis conditions.^{31–36} In addition, lithium niobates have been proven to be excellent interface materials for ASSBs.^{37,38} In this work, we realize lithium niobium oxide (LNO) thin film deposition with lithium *tert*-butoxide (LiO^tBu) as the Li source and niobium ethoxide [$\text{Nb}(\text{OEt})_5$] as the Nb source. Different ratios of Li to Nb subcycles presented thin films with different stoichiometries. Local electronic structures of the as-deposited thin films were studied by X-ray absorption near edge spectroscopy (XANES). Furthermore, the ionic conductivities of the ALD lithium niobium oxide thin films were measured.

EXPERIMENTAL SECTION

Lithium niobium oxide thin films were deposited using a Savannah 100 ALD system (Veeco/carbon nanotube (CNT) division of the Veeco Instruments Inc.). For deposition of ternary compounds, the combinations of the subcycles of lithium and niobium was used. Lithium *tert*-butoxide [LiO^tBu , $(\text{CH}_3)_3\text{COLi}$, Alfa Aesar, >99.9%] and niobium ethoxide [$\text{Nb}(\text{OEt})_5$, Et = $-\text{CH}_2\text{CH}_3$, Strem Chemicals Inc., >99.9%] were used for Li and Nb sources, respectively. Deionized water was used as the oxidant for both subcycles, and nitrogen was used as the carrier and purging gas. The system pipeline was held at 190 °C to avoid condensation of the precursors. LiO^tBu and $\text{Nb}(\text{OEt})_5$ were sublimed at 170 and 155 °C, respectively. All of the depositions were performed at a temperature of 235 °C. All of the precursors were pulsed in for 1 s, followed by 15 s of nitrogen purge. A stepwise acetone, ethanol, and water rinse procedure was applied to clean silicon (100) substrates. The cleaned substrates were then blown-dry by nitrogen. Powder-based carbon nanotubes (CNTs) were acid-treated with nitric acid (HNO_3 , 70%) for 3 h at 120 °C, followed

by washing with deionized water. After dispersing the treated CNTs in ethanol, a drop-casting method was employed on aluminum foil. The casted CNTs were dried in air overnight.

The film thicknesses were measured from the fresh-cut cross section of thin films on Si substrates using a field-emission scanning electron microscopy (SEM) (Hitachi-4800). Six spots were randomly selected on each thin film to calculate the average value as the film thickness. A low-angle X-ray diffraction (Bruker D8 Advance, Cu $K\alpha$ X-ray source) was employed to examine the phase of the thin films on Si. X-ray photoelectron spectroscopy (XPS) using a Kratos Axis Ultra Al (α) spectrometer was applied to determine the composition of the lithium niobium thin films on CNTs. The use of CNTs as substrate for XPS measurements helps to mitigate the charging effect due to the high electronic conductivity of CNTs. XANES measurements were performed on the soft X-ray microcharacterization beamline (SXRMB) endstation at Canadian light source. SXRMB endstation is equipped with a double-crystal monochromator with two sets of interchangeable crystals and the operating energy range is from 1.7 to 10 keV. A setup with the InSb(111) crystals and Si drift solid-state detector was used for the Nb L-edge XANES measurements. The detection modes were total electron yield (TEY) and X-ray fluorescence yield (FLY) with a selected energy window (e.g., Nb $L\alpha$ for Nb L_3 -edge). All of the XANES spectra were normalized to the incident photon flux and calibrated with the standard compound.

Ionic conductivities of the thin films were evaluated with electrochemical impedance spectroscopy (EIS) on a CHI electrochemistry workstation. The frequency range was from 200 kHz to 100 mHz with a temperature window of 303–373 K (10 K step). A cross-plane geometrical configuration was applied with the lithium niobium oxide thin films sandwiched between two Au electrodes. Each gold layer of ~50 nm was sputtered by a Polaron sputtering system under 2 kV for 9 min with a current of 20 mA. The geometric area of the thin film electrolytes between the two Au electrodes were $4 \times 4 \text{ mm}^2$. The EIS plots obtained were simulated using equivalent circuits and the conductivity σ could be calculated from the simulated value of the resistance. $\ln(\sigma T)$ was plotted as a function of $1000/T$. The activation energies of the thin film electrolytes were derived from the slope of the plot according to the Arrhenius equation: $\sigma T = A \exp[-E_a/(kT)]$, where T is the absolute temperature, A is the pre-exponential factor, E_a is the activation energy, and k is the Boltzmann constant.

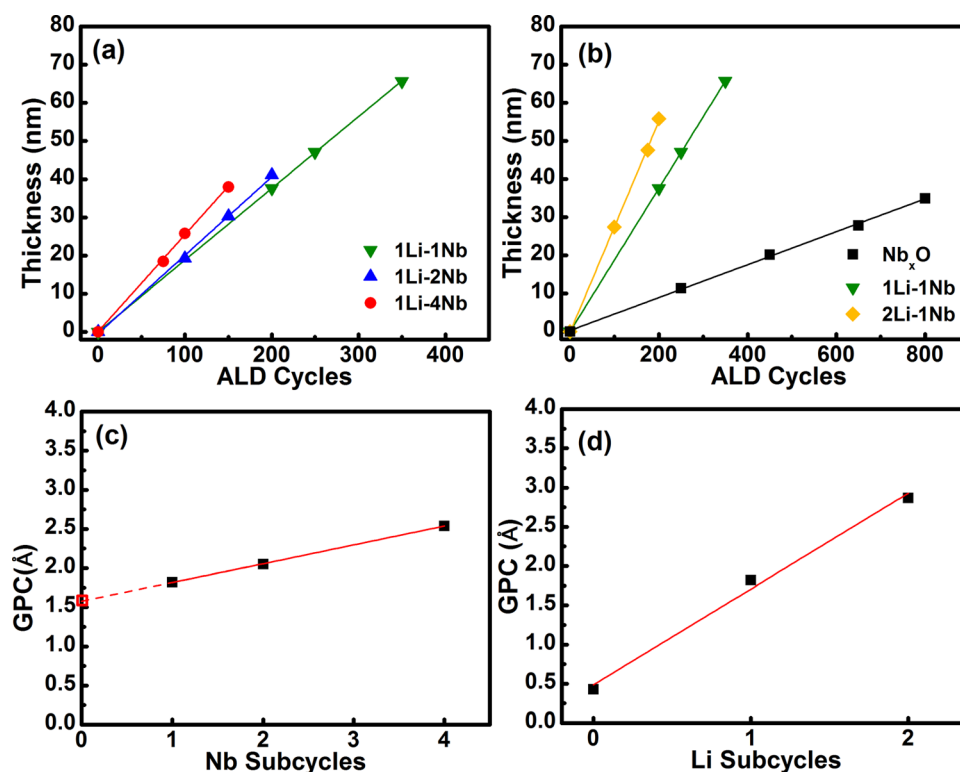


Figure 2. Thickness as a function of the number of ALD cycles for lithium niobium oxide thin films: (a) 1Li–1Nb, 1Li–2Nb, and 1Li–4Nb (Li subcycle kept as 1); (b) Nb_xO , 1Li–1Nb, and 2Li–1Nb (Nb subcycle kept as 1). GPC as a function of the number of subcycles of each component: (c) Nb subcycles (Li subcycle kept as 1) and (d) Li subcycles (Nb subcycle kept as 1).

RESULTS AND DISCUSSION

Lithium niobium oxide (LNO) thin films are deposited on CNTs and Si substrates at a deposition temperature of 235 °C, which is chosen due to the well-established temperature for deposition of niobium oxide and is within the ALD window of the lithium subcycle.^{22,27,39} Four different subcycle ratios of Li and Nb are studied: 1:1, 1:2, 1:4, and 2:1, respectively. The corresponding thin films are henceforth designated as 1Li–1Nb, 1Li–2Nb, 1Li–4Nb, and 2Li–1Nb. A complete round of deposition of both components (Li and Nb) is one full ALD cycle. For instance, one ALD cycle for 1Li–4Nb consists of one subcycle of Li and four subcycles of Nb. It is worth mentioning that Østreg et al. reported that LNO deposition by ALD could only be done after an extra 2000 cycles of niobium oxide deposition due to the reservoir effect.³⁹ However, no niobium oxide deposition is required between consecutive LNO depositions using the recipes established here, which could be attributed to the change in precursor and longer purge time. SEM images of Figure 1a,b show the resulting morphology of thin film deposition of 1Li–1Nb on CNTs after 250 ALD cycles. A conformal coating is presented on the surface of CNTs. It can be clearly seen that the CNTs are uniformly wrapped by LNO films, indicating that LNO can be deposited on high-aspect-ratio substrates. The cross-sectional views of LNO thin films on Si substrates are displayed in Figure 1c–f, where the LNO coating is highlighted with red arrows. Extremely uniform depositions are obtained for all four recipes.

The thickness of the LNO thin films is plotted against the ALD cycle number in Figure 2a,b. The measured thicknesses are linearly fitted and the slopes of the lines are the growth per cycle (GPC) ALD.^{17,40} With no lithium subcycles, the GPC for niobium oxide (denoted as Nb_xO) is 0.43 Å, which is consistent

with the results reported by Østreg et al.^{39,41} The linear behavior is maintained after combination of the Li and Nb subcycles. Furthermore, self-saturated growth is observed in 1Li–1Nb when using higher pulse time (2 s) of Li and Nb precursors, which is indicative of ALD-type growth. The GPC for 1Li–1Nb, 1Li–2Nb, 1Li–4Nb, and 2Li–1Nb is 1.82, 2.05, 2.54, and 2.87 Å, respectively, which is in agreement with the thickness measurements seen in Figure 1c–f. The obtained growth rates are of the similar magnitude as in the work of Østreg et al. despite the different Li-precursor used. Furthermore, when the GPC is a function of the subcycle number as shown in Figure 2c, one can see that the GPC increases monotonously with the number of Nb subcycles when the Li subcycle is kept constant. The y-axis intercept represents the extracted GPC of solely Li_2O in the Li subcycle (~1.6 Å), which is in accordance with previously reported values.^{21,22} The same trend can be observed in Figure 2d, where the GPC increases linearly with the number of Li subcycles when the Nb subcycle is held constant at 1. Therefore, it is suggested that the GPC of lithium niobium oxide thin films is a linear combination of the Li and niobium oxide subcycles. The reason for this behavior could be the Li subcycle, where the surface species generated after the water pulse are proposed to be hydroxide groups. Upon pulsing in $\text{Nb}(\text{OEt})_5$, a reaction can readily take place with the surface species (–OH). Furthermore, the Nb subcycle leads to surface species terminated with the same functional groups (–OH) so that the succeeding Li subcycle can readily proceed.²² Therefore, the growth mechanism of LNO is similar to the mechanisms of each binary oxide. Thus, the delay in growth due to the regeneration of functional groups between subcycles, which is often observed in ternary systems, could be ameliorated in this

mixed system.^{23,24} The self-saturating reactions of each subcycle gives rise to the linear correlation between the lithium niobium oxide thin film thickness and the ALD cycle number.

To study the chemical environment of the as-deposited LNO thin films, XANES at the Nb L₃-edge is conducted. The spectral features stem from the dipole excitation of core electrons to bound and quasi-bound states. Information associated with the local structure and bonding environment of the absorbing atom could be provided. The L-edge absorptions of Nb arise from allowed dipole $2p^{6}4d^n \rightarrow 2p^{5}4d^{n+1}$ transitions. Spin-orbit coupling of the core hole causes the splitting of the L-edge absorption into L₃ and L₂ edges, separated by roughly 94 eV. The L₃-edge involves transitions from $2p_{3/2}$ into mostly $4d_{5/2}$ final states with some $4d_{3/2}$ weighting.^{42–44}

Three standard powder samples are studied as references including LiNbO₃, Nb₂O₅, and metallic Nb (Figure 3a).

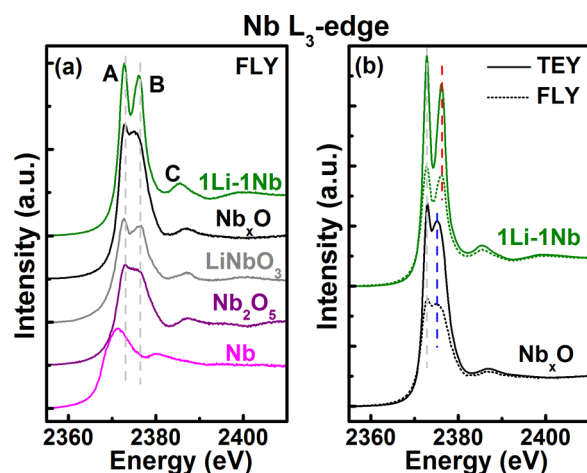


Figure 3. Nb L₃-edge XANES spectra: (a) fluorescent yield (FLY) XANES spectra of ALD thin films and standard powders (LiNbO₃, Nb₂O₅, and Nb); (b) total electron yield (TEY) and FLY XANES spectra of 1Li–1Nb and Nb_xO thin films.

Compared to the Nb L₃-edge absorption-edge spectrum of metallic Nb, which exhibits only one strong resonance, a double-peaked edge structure (peaks A and B) is well resolved in the spectra of the standard oxides. This distinctive characteristic arises from the interaction of Nb with surrounding oxygen in the compound. A relative weak feature (peak C) sitting at higher energies is attributed to the transitions from $2p_{3/2}$ to the Nb 5s state.⁴⁵ Additionally, a chemical shift to higher oxidation states can be verified by the blue-shift of the edge jump threshold energy in the spectra of the oxides. The area under the curve of the whiteline (resonance at the edge) relative to the edge jump also increases significantly in the oxides, confirming the expected depletion of Nb 4d character in the oxides.

Peak A of all of the standard oxides is well aligned at 2372.8 eV, whereas that of metallic Nb is 1.4 eV lower at 2371.4 eV. Peaks A and B track the densities of states of Nb 4d character associated with the local symmetry. Peak A of 1Li–1Nb and Nb_xO thin films occurs at the same energy position at 2372.8 eV, with no observable shift, suggesting that Nb in 1Li–1Nb and Nb_xO is at the same oxidation state (Nb⁵⁺) as in Nb₂O₅ and LiNbO₃. Furthermore, the spectral features of the ALD-deposited thin films closely resemble those of Nb₂O₅ and LiNbO₃. The double-feature observed above the edge jump stems from the ligand field splitting of d-orbitals originating

from the local coordination of Nb⁵⁺. In addition, the relative peak intensities can be utilized to identify the unit structure as tetrahedral NbO₄ or octahedral NbO₆, where peak A would be of smaller intensity as peak B in the case of the tetrahedral unit. To supplement this information, the energy gap between the two peaks corresponds to the ligand field splitting, where the value of the gap of octahedral coordination is greater than that of tetrahedral coordination.^{45,46} Furthermore, the as-deposited thin films lack long-range order because no diffraction patterns are found in low-angle X-ray diffraction. When examined closer, Nb atoms are revealed to be bonded with six oxygen atoms in octahedral structures, as implied by the XANES spectra. Therefore, it can be claimed that the Nb atoms in the ALD thin films exist as Nb⁵⁺ in octahedron units.^{42,45–47}

Interestingly, there are some subtle differences in peak positions, as summarized in Table 1. First, one can find that

Table 1. Positions (in eV) of the Peak Maximum in the Nb L₃-Edge XANES Spectra

	peak A	peak B	peak C
1Li–1Nb	2372.8	2376.1	2385.5
Nb _x O	2372.8	2375.2	2386.8
LiNbO ₃	2372.8	2376.5	2387.3
Nb ₂ O ₅	2372.8	2376.4	2387.2
Nb	2371.4		2380.2

peak B of the Nb_xO thin film in Figure 3a shifts to about 1.2 eV lower energy (2375.2 eV), compared to that of bulk Nb₂O₅ (2376.5 eV). However, when introducing the Li component into the ALD process, peak B of 1Li–1Nb shows a blue-shift to 2376.1 eV, which is still 0.4 eV lower than that of LiNbO₃. Moreover, peaks A and B are more clearly resolved in the spectrum of 1Li–1Nb than that of Nb_xO, which is similar to the conclusion when comparing the spectra of Nb₂O₅ and LiNbO₃. Additionally, peak C of both 1Li–1Nb and Nb_xO shifts to lower energy compared to Nb₂O₅ and LiNbO₃. Figure 3b presents the spectra of 1Li–1Nb and Nb_xO collected in total electron yield (TEY) and fluorescence yield (FLY) mode. TEY measures the total yield of secondary electrons (dominant), photoelectrons, and Auger electrons from the top few nanometers of the sample surface. On the other hand, FLY detects outgoing fluorescent X-rays and is considered as relatively bulk sensitive.⁴⁸ The peak positions in TEY and FLY spectra coincide very well, as marked by the dashed lines for each sample. Apart from the energy shifts of peaks B and C, the TEY spectra of 1Li–1Nb and Nb_xO demonstrate the same patterns as the FLY, where the degree of the whiteline splitting is more apparent in the lithium-containing sample. Compared to the TEY spectra, the dampening of the split in the FLY spectra could be correlated to self-absorption (the thickness effect), where the fluorescence photons are reabsorbed by the thin films.⁴⁴ Nevertheless, the resemblance of the TEY and FLY spectra suggests similar electronic structure of Nb at the surface and in the bulk of the LNO thin films.

The above discerned differences are a reflection of the fact that local, instead of long-range interactions, dominate in the ALD LNO thin films. The presence of Li and O atoms around the Nb atoms leads to orbital hybridizations, modifying the local environment in the complex. In the context of a molecular orbital scheme, the origin of peaks A and B can be ascribed to the transitions from the Nb $2p_{3/2}$ level to the unoccupied $2t_{2g}(\pi^*)$ and $3e_g(\sigma^*)$, in addition to the allowed transitions to the

empty $3a_{1g}$ (σ^*) at peak C.^{45,46} In the case here, octahedral units constitute both the standards and the thin films. Although sustained in the same symmetry, the distortion might involve a change in the metal–oxygen bond length or orientation.⁴⁷ In standard LiNbO_3 and Nb_2O_5 , the Nb atoms exist in perfectly coordinated octahedrons, whereas in the corresponding ALD thin films, they are found to be in a distorted octahedral environment and thus lower the energy level of the empty $3a_{1g}$ (σ^*) state. As reported in literatures, the least distortion generates the largest splitting (A–B separation), as shown in the spectra of the standard samples.^{45,47,49,50} Henceforth, it is proposed that the Nb and O atoms are packed into a distorted octahedral symmetry in the ALD process, most likely owing to the fact that only amorphous phase is formed at the relatively low deposition temperature. When taking into consideration the radius difference between Li^+ and Nb^{5+} , the octahedron skeleton is unlikely to be changed by the introduction of Li subcycles. In addition, previous studies have shown that when the supporting surface is a basic environment, the niobium oxide can interact with the support and result in the formation of highly distorted NbO_6 octahedron. In other words, the hydroxide groups readily formed on the surface between the Li and Nb ALD subcycles could help facilitate the formation of the distortion.⁵¹ Comparing the spectra of 1Li–1Nb and Nb_xO , octahedrons in both samples were distorted, but to different degree, due to the insertion of the lithium ions. It is possible that the distortion was alleviated and, thus, peaks A and B were more separated for 1Li–1Nb.^{45,47,49,50}

XANES studies of the thin films with varying number of subcycles (Figure 4) illustrate that the double-peaked whiteline

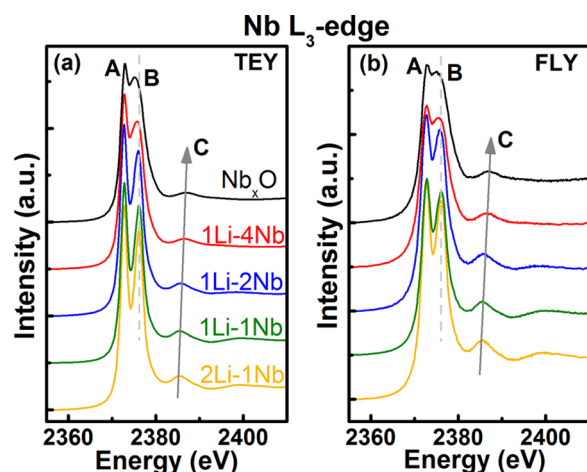


Figure 4. Nb L_3 -edge XANES spectra of Nb_xO , 1Li–4Nb, 1Li–2Nb, 1Li–1Nb, and 2Li–1Nb in (a) TEY mode and (b) FLY mode.

and the subsequent weak peak were preserved in the spectra (both TEY and FLY) of all of the materials. Taking a closer look at Figure 4a, the position of peak A remains constant at 2372.8 eV. The relative peak intensity of peaks A and B, and the value of the peak separation manifest that the octahedral symmetry is persistent in the as-deposited thin films in spite of the changing subcycle ratio. More strikingly, an apparent trend of evolution of the spectra is found. The separation of peaks A and B becomes narrower and the relative intensity of the gap between peaks A and B is gradually increased with a lower Li-to-Nb subcycle ratio from 2 (2Li–1Nb) down to 0 (Nb_xO), accompanied by a continuing blue-shift of peak C. The red-shift

of peak B is rather delicate (0.1 eV) from 2Li–1Nb to 1Li–1Nb, but reaches 0.5 eV in the spectra of 1Li–4Nb. In theory, the addition of more Li subcycles leads to the incorporation of more Li atoms in the film composition. As discussed above, the degree of the distortion of the octahedral symmetry accounts for the shift in peak B. Thus, it is indicative that the octahedrons experience the strongest distortion in the Nb_xO thin film, whereas the distortion is mitigated to some extent with the increasing amount of Li content in the LNO thin films. In addition, the degree of the splitting should be a sign of the ability of the ligand to split the energy levels.^{49,50} The less-contrasted gap between the t_{2g} and e_g levels could possibly mean that there is an increase in the probability of the transitions to the empty space between the $2t_{2g}$ (π^*) and $3e_g$ (σ^*) states and a change in the degeneracy of the molecular orbitals. The continuing shift in peak C implies that the empty state $3a_{1g}$ (σ^*) is elevated to a higher energy level, related to the distortion with reducing lithium content in the thin films.^{45,52} More importantly, the excellent agreement of the TEY and the corresponding FLY spectrum substantiates that the prominent phenomenon observed in the XANES study takes place not only on the surface but also in the bulk of the thin films.

The above-discussed notions are on the basis that higher ratios of Li to Nb subcycles deliver higher lithium content in the thin films. To verify this, the elemental composition was determined by XPS. Figure 5a provides the survey scans of the as-deposited LNO thin films, showing the presence of Li in the thin films. The appearance of carbon signal should be due to the CNT substrates. XPS is rather a surface-sensitive technique that probes the quantity of chemical species in the regime close to the sample surface. A clear trend could still be obtained by comparing the data from the thin films in terms of the relative Li and Nb content in the surface region. It is reasonable to conclude that the overall Li-to-Nb content ratio follows the same trend, whereas depth profile would be an effective approach for further detailed compositional analysis. Figure 5b lists the atomic ratio of Li to Nb in the 1Li–4Nb, 1Li–2Nb, 1Li–1Nb, and 2Li–1Nb thin films, respectively, indicating that the lithium content increased with the higher ratio of Li to Nb subcycles. High-resolution XPS spectra of Li 1s are depicted in Figure 5c–f, with deconvolutions of the 1s peaks. Only one sharp and symmetric peak can be detected at 55.0 ± 0.1 eV in all four LNO thin films, revealing a single chemical state of Li^+ in each sample. The peak at higher binding energy belongs to the Nb 4s. The single peak can be attributed to the bonding state of Li–O–Nb as exemplified by lithium niobate glasses found in the literatures.^{53–55} The consistent peak position of Li 1s for the four LNO thin films elucidates that Li shares a similar chemical environment in the thin films with different ratios of Li to Nb subcycles.

Ionic conductivity of the LNO thin films are evaluated by EIS using a cross-plane configuration. The Cole–Cole plot of 1Li–4Nb acquired at temperatures ranging from 303 to 353 K, with the equivalent circuit used to fit the data, is displayed in Figure 6a. The impedance plots of 1Li–1Nb, 1Li–2Nb, and 2Li–1Nb were also constructed (Supporting Information). Each complex impedance curve consists of a semicircle at high frequency, which corresponds to the bulk resistance of the LNO thin films. An inclined tail can be noticed in the low-frequency region due to the polarization of the electrode–electrolyte interface. Taken together, the behavior is representative of an ionic conductor in an open circuit with an ionic blocking electrode (Au in this case).^{22,24,27} In the equivalent circuit, R_0 is the contact ohmic

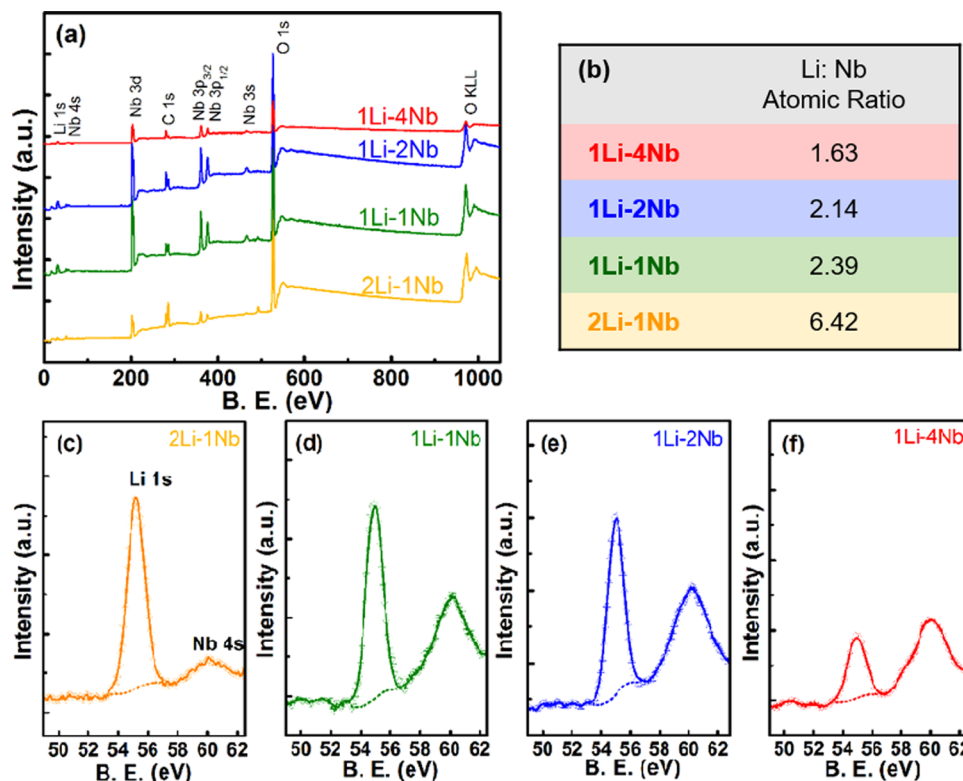


Figure 5. XPS spectra of the four LNO thin films on CNTs substrates: (a) survey scans; (b) compositional ratio of Li to Nb; and (c–f) deconvolution of Li 1s spectra.

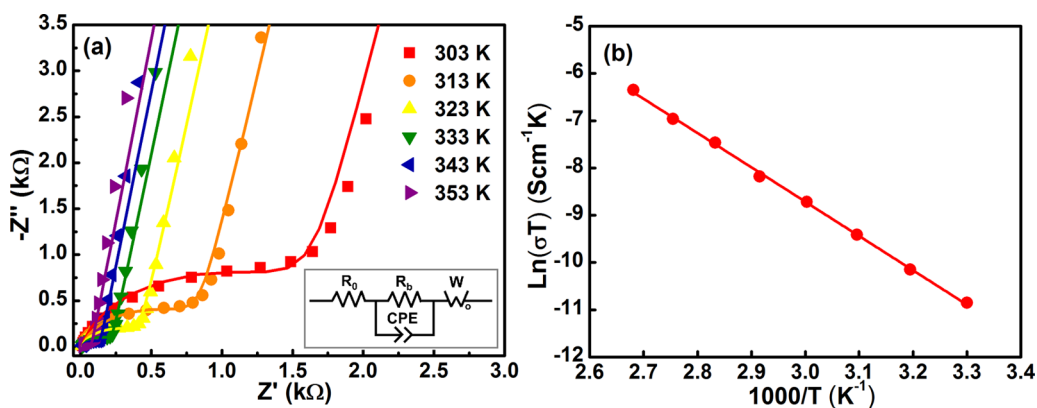


Figure 6. (a) Impedance plot of 1Li-4Nb thin film and (inset: equivalent circuit) and (b) Arrhenius plots of the ionic conductivity of 1Li-4Nb thin film measured between 303 and 353 K. (Scattered points are measured values and solid lines are fitted results.)

resistance and the constant-phase element defines the bulk capacitance of the LNO thin films. W denotes the finite length Warburg element, applicable when charge carriers diffuse through a solid. The ionic conductivity of the LNO thin films were calculated using the fitted bulk resistance (denoted as R_b). The equation, $\sigma = d/(AR_b)$, was employed, wherein d is the thickness of the LNO thin film and A is the geometric area of the lithium niobium oxide thin films between the Au electrodes. 1Li-4Nb thin film exhibited the best ionic conductivity among the four LNO thin films, which reached $6.39 \times 10^{-8} \text{ S cm}^{-1}$ at 303 K and $1.62 \times 10^{-6} \text{ S cm}^{-1}$ at 353 K. The Arrhenius plot in Figure 6b demonstrates the ionic conductivity at varying temperatures. The activation energy, E_a , was derived from the equation, $\sigma T = \sigma_c \exp[-E_a/(kT)]$, where σ_c is a constant, k is the Boltzmann constant, and T is the absolute temperature. An

activation energy of 0.62 eV for 1Li-4Nb thin film was extracted from the slope of the linear fitted line, which is the lowest of the four LNO thin films. The conductivity achieved is comparable to that of thin films prepared by sputtering, and the activation energy falls into the range of reported values of lithium niobate glasses.^{31,33,35,36} The LNO thin films by ALD can provide a moderate ionic conductivity at room temperature, which is even higher than that of other similar amorphous systems developed by ALD such as lithium aluminum oxide, lithium tantalum oxide, and lithium phosphate.^{21,22,24,27} This promises the possibility of the implementation of lithium niobium oxide thin films developed by ALD as a solid-state electrolyte in all-solid-state batteries.

CONCLUSIONS

In this study, we have demonstrated a viable ALD process to deposit lithium niobium oxide thin films by combining Li (LiO^tBu and H₂O) and Nb [Nb(OEt)₅ and H₂O] subcycles at a deposition temperature of 235 °C. Self-limiting behavior and uniform growth on different substrates were achieved with ALD recipes composed of various subcycle ratios. Different ratios of Li to Nb subcycles could provide a tunable composition, which in turn affected the electrochemical performances and the local electronic structures. For the first time, detailed XANES studies of the ALD niobium oxide and LNO thin films were carried out with a focus on the Nb L₃-edge. Despite the fact that the as-deposited thin films were amorphous and lacked long-range order, local octahedral units of NbO₆ were shown to be the building blocks of the thin films. XANES analysis indicated that the Nb in Nb_xO and LNO thin films exists as Nb⁵⁺, and the degree of distortion in the octahedral structure is dependent on the ALD subcycle ratio. Furthermore, it was found that the Nb_xO thin film exhibited the most distortion, and it was shown that the distortion can be decreased to some extent with the addition of lithium content by increasing the Li-to-Nb subcycle ratio. The TEY and FLY spectra confirmed the consistency of the electronic structure on the surface and in the bulk of the ALD thin films. Moreover, the as-grown LNO thin film with a Li/Nb subcycle ratio of 1:4 delivered a Li⁺ conductivity of 6 × 10⁻⁸ S cm⁻¹ at room temperature, which provides great promise for future application as a solid-state electrolyte and interfacial engineering material in solid-state batteries.

ASSOCIATED CONTENT

Supporting Information

The Supporting Information is available free of charge on the ACS Publications website at DOI: 10.1021/acsami.7b13467.

Impedance plot of (a) 1Li–2Nb, (b) 1Li–1Nb, (c) 2Li–1Nb thin films, and (d) Arrhenius plots of the ionic conductivity of the three thin films measured between 303 and 353 K (PDF)

AUTHOR INFORMATION

Corresponding Authors

*E-mail: tsham@uwo.ca. Tel: +1 519 661 2111 ext 86341 (T.-K.S.).

*E-mail: xsun@eng.uwo.ca. Tel: +1 519 661 2111 ext 87759 (X.S.).

ORCID

Yang Zhao: 0000-0002-4148-2603

Xueliang Sun: 0000-0003-2881-8237

Notes

The authors declare no competing financial interest.

ACKNOWLEDGMENTS

This work was supported by the Nature Sciences and Engineering Research Council of Canada (NSERC), the Canada Research Chairs, the Canada Foundation for Innovation (CFI), the Ontario Research Fund, Canada Light Source at the University of Saskatchewan, and Surface Science at the University of Western Ontario. The Canadian Light Source was supported by CFI, NSERC, NRC, CIHR, and the University of Saskatchewan.

REFERENCES

- (1) Goodenough, J. B.; Park, K.-S. The Li-Ion Rechargeable Battery: A Perspective. *J. Am. Chem. Soc.* **2013**, *135*, 1167–1176.
- (2) Erickson, E. M.; Ghanty, C.; Aurbach, D. New Horizons for Conventional Lithium Ion Battery Technology. *J. Phys. Chem. Lett.* **2014**, *5*, 3313–3324.
- (3) Manthiram, A. Materials Challenges and Opportunities of Lithium Ion Batteries. *J. Phys. Chem. Lett.* **2011**, *2*, 176–184.
- (4) Crabtree, G. The Energy-Storage Revolution. *Nature* **2015**, *526*, No. S92.
- (5) Quartarone, E.; Mustarelli, P. Electrolytes for Solid-State Lithium Rechargeable Batteries: Recent Advances and Perspectives. *Chem. Soc. Rev.* **2011**, *40*, 2525–2540.
- (6) Zhu, Y.; He, X.; Mo, Y. Origin of Outstanding Stability in the Lithium Solid Electrolyte Materials: Insights from Thermodynamic Analyses Based on First-Principles Calculations. *ACS Appl. Mater. Interfaces* **2015**, *7*, 23685–23693.
- (7) Bachman, J. C.; Mui, S.; Grimaud, A.; Chang, H. H.; Pour, N.; Lux, S. F.; Paschos, O.; Maglia, F.; Lupart, S.; Lamp, P.; Giordano, L.; Shao-Horn, Y. Inorganic Solid-State Electrolytes for Lithium Batteries: Mechanisms and Properties Governing Ion Conduction. *Chem. Rev.* **2016**, *116*, 140–162.
- (8) Sun, C.; Liu, J.; Gong, Y.; Wilkinson, D. P.; Zhang, J. Recent Advances in All-Solid-State Rechargeable Lithium Batteries. *Nano Energy* **2017**, *33*, 363–386.
- (9) Oudenhoven, J. F. M.; Baggetto, L.; Notten, P. H. L. All-Solid-State Lithium-Ion Microbatteries: A Review of Various Three-Dimensional Concepts. *Adv. Energy Mater.* **2011**, *1*, 10–33.
- (10) Yang, Y.; Peng, Z.; Wang, G.; Ruan, G.; Fan, X.; Li, L.; Fei, H.; et al. Three-Dimensional Thin Film for Lithium-Ion Batteries and. *ACS Nano* **2014**, *8*, 7279–7287.
- (11) Ferrari, S.; Loveridge, M.; Beattie, S. D.; Jahn, M.; Dashwood, R. J.; Bhagat, R. Latest Advances in the Manufacturing of 3D Rechargeable Lithium Microbatteries. *J. Power Sources* **2015**, *286*, 25–46.
- (12) Zhang, Y.; Lai, J.; Gong, Y.; Hu, Y.; Liu, J.; Sun, C.; Wang, Z. L. A Safe High-Performance All-Solid-State Lithium-Vanadium Battery with a Freestanding V₂O₅ Nanowire Composite Paper Cathode. *ACS Appl. Mater. Interfaces* **2016**, *8*, 34309–34316.
- (13) Liu, C.; Gillette, E. I.; Chen, X.; Pearce, A. J.; Kozen, A. C.; Schroeder, M. A.; Gregorczyk, K. E.; Lee, S. B.; Rubloff, G. W. An All-in-One Nanopore Battery Array. *Nat. Nanotechnol.* **2014**, *9*, 1031–1039.
- (14) Pearce, A. J.; Schmitt, T. E.; Fuller, E. J.; El-Gabaly, F.; Lin, C. F.; Gerasopoulos, K.; Kozen, A. C.; Talin, A. A.; Rubloff, G.; Gregorczyk, K. E. Nanoscale Solid State Batteries Enabled by Thermal Atomic Layer Deposition of a Lithium Polyphosphazene Solid State Electrolyte. *Chem. Mater.* **2017**, *29*, 3740–3753.
- (15) Meng, X.; Wang, X.; Geng, D.; Ozgit-Akgun, C.; Schneider, N.; Elam, J. W. Atomic Layer Deposition for Nanomaterials Synthesis and Functionalization in Energy Technology. *Mater. Horiz.* **2017**, *4*, 133–154.
- (16) Knoop, H. C. M.; Donders, M. E.; Baggetto, L.; van de Sanden, M. C. M.; Notten, P. H. L.; Kessels, W. M. M. Atomic Layer Deposition for All-Solid-State 3D-Integrated Batteries. *ECS Trans.* **2009**, *25*, 333–344.
- (17) George, S. M. Atomic Layer Deposition: An Overview. *Chem. Rev.* **2010**, *110*, 111–131.
- (18) Meng, X.; Yang, X.-Q.; Sun, X. Emerging Applications of Atomic Layer Deposition for Lithium-Ion Battery Studies. *Adv. Mater.* **2012**, *24*, 3589–3615.
- (19) Liu, J.; Sun, X. Elegant Design of Electrode and Electrode/electrolyte Interface in Lithium-Ion Batteries by Atomic Layer Deposition. *Nanotechnology* **2015**, *26*, No. 024001.
- (20) Putkonen, M.; Aaltonen, T.; Alnes, M.; Sajavaara, T.; Nilsen, O.; Fjellvåg, H. Atomic Layer Deposition of Lithium Containing Thin Films. *J. Mater. Chem.* **2009**, *19*, 8767–8771.

- (21) Aaltonen, T.; Nilsen, O.; Magrasó, A.; Fjellvåg, H. Atomic Layer Deposition of $\text{Li}_2\text{O}-\text{Al}_2\text{O}_3$ Thin Films. *Chem. Mater.* **2011**, *23*, 4669–4675.
- (22) Liu, J.; Banis, M. N.; Li, X.; Lushington, A.; Cai, M.; Li, R.; Sham, T.-K.; Sun, X. Atomic Layer Deposition of Lithium Tantalate Solid-State Electrolytes. *J. Phys. Chem. C* **2013**, *117*, 20260–20267.
- (23) Aaltonen, T.; Alnes, M.; Nilsen, O.; Costelle, L.; Fjellvåg, H. Lanthanum Titanate and Lithium Lanthanum Titanate Thin Films Grown by Atomic Layer Deposition. *J. Mater. Chem.* **2010**, *20*, 2877–2881.
- (24) Kazyak, E.; Chen, K. H.; Wood, K. N.; Davis, A. L.; Thompson, T.; Bielinski, A. R.; Sanchez, A. J.; Wang, X.; Wang, C.; Sakamoto, J.; Dasgupta, N. P. Atomic Layer Deposition of the Solid Electrolyte Garnet $\text{Li}_7\text{La}_3\text{Zr}_2\text{O}_{12}$. *Chem. Mater.* **2017**, *29*, 3785–3792.
- (25) Perng, Y.-C.; Cho, J.; Membreno, D.; Cirigliano, N.; Dunn, B.; Chang, J. P.; et al. Synthesis of Ion Conducting $\text{Li}_x\text{Al}_y\text{Si}_z\text{O}$ Thin Films by Atomic Layer Deposition. *J. Mater. Chem. A* **2014**, *2*, 9566–9573.
- (26) Cao, Y.; Meng, X.; Elam, J. W. Atomic Layer Deposition of $\text{Li}_x\text{Al}_y\text{S}$ Solid-State Electrolytes for Stabilizing Lithium-Metal Anodes. *ChemElectroChem* **2016**, *3*, 858–863.
- (27) Wang, B.; Liu, J.; Sun, Q.; Li, R.; Sham, T.; et al. Atomic Layer Deposition of Lithium Phosphates as Solid-State Electrolytes for All-Solid-State Microbatteries. *Nanotechnology* **2014**, *25*, No. 504007.
- (28) Nisula, M.; Shindo, Y.; Koga, H.; Karppinen, M. Atomic Layer Deposition of Lithium Phosphorus Oxynitride. *Chem. Mater.* **2015**, *27*, 6987–6993.
- (29) Kozen, A. C.; Pearse, A. J.; Lin, C.; Noked, M.; Rubloff, G. W. Atomic Layer Deposition of the Solid Electrolyte LiPON. *Chem. Mater.* **2015**, *27*, 5324–2331.
- (30) Shibata, S. Thermal Atomic Layer Deposition of Lithium Phosphorus Oxynitride as a Thin-Film Solid Electrolyte. *J. Electrochem. Soc.* **2016**, *163*, A2555–A2562.
- (31) Benaissa, K.; et al. Electrical and Optical Properties of LiNbO_3 . *Thin Solid Films* **1992**, *214*, 219–222.
- (32) Glass, A. M.; Nassau, K.; Negran, T. J. Ionic Conductivity of Quenched Alkali Niobate and Tantalate Glasses. *J. Appl. Phys.* **1978**, *49*, 4808–4811.
- (33) Can, N.; Ashrit, P. V.; Bader, G.; Girouard, F.; Truong, V. Van. Electrical and Optical Properties of Li-Doped LiBO_2 and LiNbO_3 Films. *J. Appl. Phys.* **1994**, *76*, 4327–4331.
- (34) Özer, N.; Lampert, C. M. Electrochemical Lithium Insertion in Sol-Gel Deposited LiNbO_3 Films. *Sol. Energy Mater. Sol. Cells* **1995**, *39*, 367–375.
- (35) Nguyen, L. Q.; Chen, L.; Truong, V.-V. A Novel Lithium Conductor Prepared by Unbalanced Magnetron R.f. Sputtering. *Thin Solid Films* **1997**, *293*, 175–178.
- (36) Xia, H.; Wang, H. L.; Xiao, W.; Lai, M. O.; Lu, L. Thin Film Li Electrolytes for All-Solid-State Micro-Batteries. *Int. J. Surf. Sci. Eng.* **2009**, *3*, 23–43.
- (37) Takada, K.; Ohta, N.; Zhang, L.; Fukuda, K.; Sakaguchi, I.; Ma, R.; Osada, M.; Sasaki, T. Interfacial Modification for High-Power Solid-State Lithium Batteries. *Solid State Ionics* **2008**, *179*, 1333–1337.
- (38) Ohta, N.; Takada, K.; Sakaguchi, I.; Zhang, L.; Ma, R.; Fukuda, K.; Osada, M.; Sasaki, T. LiNbO_3 -Coated LiCoO_2 as Cathode Material for All Solid-State Lithium Secondary Batteries. *Electrochem. Commun.* **2007**, *9*, 1486–1490.
- (39) Østreng, E.; Sonstebj, H. H.; Sajavaara, T.; Nilsen, O.; Fjellvåg, H. Atomic Layer Deposition of Ferroelectric LiNbO_3 . *J. Mater. Chem. C* **2013**, *1*, 4283–4290.
- (40) Leskelä, M.; Ritala, M. Atomic Layer Deposition Chemistry: Recent Developments and Future Challenges. *Angew. Chem., Int. Ed.* **2003**, *42*, 5548–5554.
- (41) Kukli, B. K.; Ritala, M.; Leskelä, M.; Lappalainen, R. Niobium Oxide Thin Films Grown by Atomic Layer Epitaxy. *Chem. Vap. Deposition* **1998**, *4*, 29–34.
- (42) Gianetti, T. L.; Nocton, G.; Minasian, S. G.; Tomson, N. C.; Kilcoyne, A. L. D.; Kozimor, S. A.; Shuh, D. K.; Tylliszczak, T.; Bergman, R. G.; Arnold, J. Diniobium Inverted Sandwich Complexes with Mu-eta6:eta6-Arene Ligands: Synthesis, Kinetics of Formation, and Electronic Structure. *J. Am. Chem. Soc.* **2013**, *135*, 3224–3236.
- (43) Gianetti, T. L.; Nocton, G.; Minasian, S. G.; Kaltsoyannis, N.; Kilcoyne, A. L. D.; Kozimor, S. A.; Shuh, D. K.; Tylliszczak, T.; Bergman, R. G.; Arnold, J. Electron Localization in a Mixed-Valence Diniobium Benzene Complex. *Chem. Sci.* **2015**, *6*, 993–1003.
- (44) Ruckman, M. W.; Reisfeld, G.; Jisrawi, N. M.; Weinert, M.; Strongin, M.; Wiesmann, H.; Croft, M.; Sahiner, A.; Sills, D.; Ansari, P. XANES Study of Hydrogen Incorporation in a Pd-Capped Nb Thin Film. *Phys. Rev. B* **1998**, *57*, 3881–3886.
- (45) Sugiura, C.; Kitamura, M.; Muramatsu, S. Niobium L3 and L2 X-Ray Absorption-Edge Spectra of Nb_2O_5 and NH_4NbF_6 . *J. Phys. Chem. Solids* **1988**, *49*, 1095–1099.
- (46) Kubouchi, Y.; Hayakawa, S.; Namatame, H.; Hirokawa, T. Direct Observation of Fractional Change of Niobium Ionic Species in a Solution by Means of X-Ray Absorption Fine Structure Spectroscopy. *X-Ray Spectrom.* **2012**, *41*, 259–263.
- (47) Cao, J.; Poumellec, B.; Mazerolles, L.; Brisset, F.; Helbert, A. L.; Surble, S.; He, X.; Lancry, M.; Pinckney, L. Nanoscale Phase Separation in Lithium Niobium Silicate Glass by Femtosecond Laser Irradiation. *J. Am. Ceram. Soc.* **2017**, *100*, 115–124.
- (48) Zhang, Y. F.; Liao, L. S.; Chan, W. H.; Lee, S. T.; Sammynaiken, R.; Sham, T. K.; Si, T. Electronic Structure of Silicon Nanowires: A Photoemission and X-Ray Absorption Study. *Phys. Rev. B* **2000**, *61*, No. 8298.
- (49) Bare, S. R.; Mitchell, G. E.; Maj, J. J.; Vrieland, G. E.; Gland, J. L. Local Site Symmetry of Dispersed Molybdenum Oxide Catalysts: XANES at the Mo L_{2,3}-Edges. *J. Phys. Chem.* **1993**, *97*, 6048–6053.
- (50) Hu, H.; Wachs, I. E.; Bare, S. R. Surface Structures of Supported Molybdenum Oxide Catalysts: Characterization by Raman and Mo L₃-Edge XANES. *J. Phys. Chem.* **1995**, *99*, 10897–10910.
- (51) Nowak, I.; Ziolk, M. Niobium Compounds: Preparation, Characterization, and Application in Heterogeneous Catalysis. *Chem. Rev.* **1999**, *99*, 3603–3624.
- (52) Nuraini, U.; Agustianawati, D.; Yahya, E.; Cahyono, Y.; Kidkhunthod, P.; Suasmoro, S. The Influence of Local Distortion on the Electrical Properties of the $(1-x)(\text{K}_{0.5}\text{Na}_{0.5})\text{NbO}_3-x(\text{Ba}_{0.8}\text{C}_{0.2})\text{TiO}_3$ System. *Ceram. Int.* **2017**, *43*, 3664–3669.
- (53) Özer, N.; Rubin, M. D.; Lampert, C. M. Optical and Electrochemical Characteristics of Niobium Oxide Films Prepared by Sol-Gel Process and Magnetron Sputtering A Comparison. *Sol. Energy Mater. Sol. Cells* **1996**, *40*, 285–296.
- (54) Aufray, M.; Menuel, S.; Fort, Y.; Eschbach, J.; Rouxel, D.; Vincent, B. New Synthesis of Nanosized Niobium Oxides and Lithium Niobate Particles and Their Characterization by XPS Analysis. *J. Nanosci. Nanotechnol.* **2009**, *9*, 4780–4785.
- (55) Kaufher, N.; Eichorst, D. J.; Payne, D. A. X-ray Photoelectron Spectroscopy Studies of Alkoxide-derived Lithium Niobate. *J. Vac. Sci. Technol., A* **1996**, *14*, 299–306.